Computers and Fluids 229 (2021) 105087

Contents lists available at ScienceDirect

Computers and Fluids

journal homepage: www.elsevier.com/locate/compfluid

Shock wave and turbulent boundary layer interaction in a double compression ramp

Fulin Tong [a,b,c], Junyi Duan [a,d], Xinliang Li [a,d,*]

[a] LHD, Institute of Mechanics, Chinese Academy of Sciences, 100190, Beijing, China
[b] State Key Laboratory of Aerodynamics, China Aerodynamics Research and Development Center, 621000, Mianyang, China
[c] Computational Aerodynamics Institute, China Aerodynamics Research and Development Center, 621000, Mianyang, China
[d] School of Engineering Science, University of Chinese Academy of Sciences, 100049, Beijing, China

ARTICLE INFO

Keywords:
Shock wave
Turbulent boundary layer
Double compression ramp
Direct numerical simulation

ABSTRACT

Direct numerical simulations of shock wave and supersonic turbulent boundary layer interaction in a double compression ramp with fixed ramp angles of 12° and 24° at Mach 2.9 are conducted. The characteristics of the shock interactions are investigated for four different length between the two ramp kinks, corresponding to L_c = $0.9\delta_{ref}$, $1.8\delta_{ref}$, $2.7\delta_{ref}$, and $3.6\delta_{ref}$ (δ_{ref} being the upstream turbulent boundary layer thickness). The influence of increasing L_c on flow structures, unsteadiness, Reynolds stress, turbulence kinetic energy, and Reynolds stress anisotropy tensor is assessed. The size of the separation region is significantly decreased and reattached flow appears between the two ramp kinks. Streamwise vorticity contours and streamline curvature show the decreased spanwise width and increased spanwise coherency of Görtler-like vortices. Analysis of fluctuating wall pressure indicates that the low-frequency unsteadiness is strongly suppressed in the interaction region. Profiles of Reynolds stress components and turbulence kinetic energy exhibit different turbulence evolution across the interaction, leading to substantial differences observed in the anisotropy invariant map. It is found that the near wall region is characterized by decreased anisotropy, becoming closer to the axisymmetric compression state, while a significant increase of turbulence is identified in the outer region, following the axisymmetric expansion limit. Moreover, downstream of the interaction, turbulence in the near-wall region experiences a faster recovery and the influence of L_c is found to be marginal. The main effect of L_c is observed in the outer region, an increase of L_c resulting in a monotonic decay of turbulence intensities and an inward movement of turbulent structures.

1. Introduction

Owing to the crucial important in many high-speed vehicles, a wide body of experimental and numerical studies has been performed on shock wave and turbulent boundary layer interactions (SWTBLIs) in compression ramp for several decades. Remarkable advances have been made on this research field [1–2], even though there are still some open questions of great importance for in-depth studies. So far, numerous experimental and numerical works mainly focused on the effect of ramp angle. Settles *et al.* [3] experimentally investigated the development of mean flow field properties in compression ramp from attached to separated conditions. Additional experiments in Mach 2.25 supersonic compression ramps having different angles were carried out by Ardonceau [4] to focus on the longitudinal and lateral properties of turbulence structure in SWTBLIs, and a pronounced anisotropy was found after passing through the shock. Mustafa *et al.* [5] did experiments to compare the streamwise turbulent kinetic energy (sTKE) in Mach 2.8 flow over 8°, 16°, 24°, and 32° compression ramps. They observed that the wall-normal integrated sTKE scaled as an exponential with respect to the compression-ramp angels. Using direction numerical simulation (DNS), Tong *et al.* [6] examined the ramp angle effect on turbulent kinetic energy budgets in a Mach 2.9 turbulent flow, and highlighted the importance of the separated shear layer. In addition, Muck *et al.* [7] measured wall pressure fluctuations in three different two-dimensional ramp modes of corner angle 16°, 20 °, and 24 ° with flow conditions ranging from fully separated to incipient separation. They suggested that the intermittent wall pressure signals at the mean separation were dominated by the large-scale low-frequency oscillation motion of shock wave, and a marked decrease in the time scale was found in the separated region as the ramp angle was increased. Recently, Sun *et al.* [8]

* Corresponding author.
E-mail address: lixl@imech.ac.cn (X. Li).

https://doi.org/10.1016/j.compfluid.2021.105087
Received 9 February 2021; Received in revised form 6 May 2021; Accepted 19 July 2021
Available online 4 August 2021

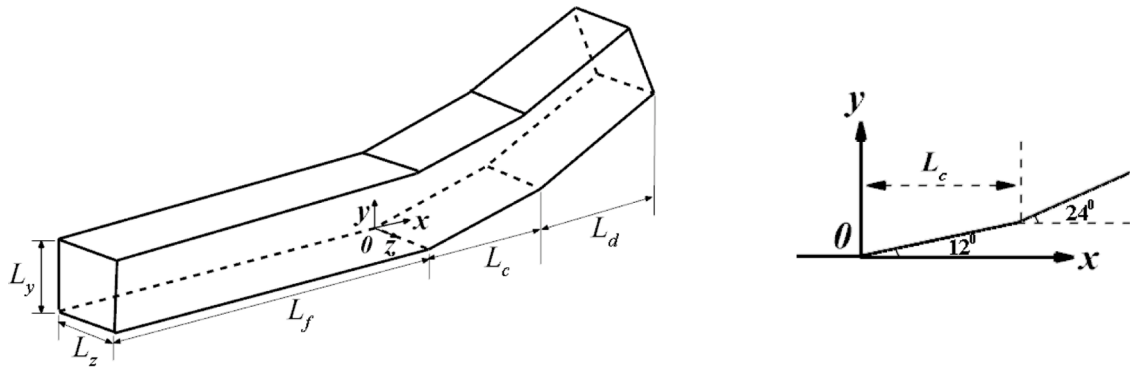

Fig. 1. (a) Sketch of the computational domain and (b) schematic of the considered double compression ramp.

experimentally studied the effect of increasing ramp angles on the low-frequency unsteadiness using high-speed schlieren, and found that a larger ramp angle gave rise to a stronger spectral intensity in the low frequency band. Many efforts have been made to address the physical mechanisms of the low-frequency unsteadiness in SWTBLIs, which is still not fully understood, as reviewed in Clemens *et al.* [9].

Despite double compression ramp frequently occurs in a scramjet inlet or control surface of high speed vehicles, little attention has been emphasized on SWTBLIs in this flow configuration. Unlike the interactions in the single compression ramp, the presence of the second ramp results in a multiple shock systems with high levels of complexity, particularly when the angle of the second ramp is large and subsequent separation occurs. Another important parameter is the length between the two ramp kinks. For short lengths, the disturbed boundary layer downstream of the first interaction, which is far from equilibrium state, immediately enters into the secondary interaction. If the length is sufficient large, the flow passing the first interaction is reattached and experiences a relax process ahead of the secondary interaction. Improving the understanding of the underlying physics associated with the double interactions can create better foundations for flow control and design process.

However, at present, there have been a relatively small number of experimental and numerical studies on double compression ramps in the literature. For example, Goldfeld *et al.* [10] performed Reynolds averaged Navier-Stokes simulations (RANS) of SWTBLIs in supersonic double compression ramps with a fixed length between the two ramps. In their simulations, the first ramp angle α_1 varied but the second ramp angle α_2 was held constant to focus on the influence of the preliminary shock on the separation properties of the second interactions. They found that the existence of the local separation in the first ramp strengthened the ability of the boundary layer to withstand separation, leading to considerably reduced separation region in the second ramp. Gaisbauer *et al.* [11] experimentally and numerically studied the influence of the distance between the two ramp kinks on the interactions in a flat-plate/double ramp configuration with fixed ramp angle $\alpha_1 = 11^o$ and $\alpha_2 = 9^o$ at Mach 2.55. They suggested that the free interaction theory, previously proposed by Chapman *et al.* [12], was still valid as long as the two ramp angles and the distance between the two ramp kinks were taken into account. To attain the minimum value of pressure drag, Fedorchenko *et al.* [13] performed RANS computations to find out optimal geometrical parameters of a supersonic double ramp configuration. It is well known that RANS calculations fail to provide information about unsteadiness and turbulence fluctuation in the shock interactions.

Nowadays, with great advances, DNS has been widely used as a powerful tool for analyzing the complex unsteady turbulent flows in SWTBLIs, due to its high-resolution. For DNS, all relevant temporal and spatial flow scales are accurately captured, and any quantity of interest can be directly provided. The DNS of compression ramp was first performed by Adam *et al.* [14], focusing on turbulence amplification mechanism and large-scale unsteady shock motion. Further, extensive computations by means of the DNS have been carried out in Martin's group [15–18] to aim at the origin of the low-frequency unsteadiness. DNS results by Zhu *et al.* [19] and Tong *et al.* [20] concluded the wall temperature effects on the behavior of a compression ramp-induced SWTBLIs. To the best of our knowledge, there are no studies making the best of DNS in analyzing fundamental mechanisms of SWTBLIs in the double compression ramp. Therefore, in this paper, we perform direct numerical simulations of SWTBLIs in a double compression ramp. The main purpose of this work is to investigate the effect of the length between the two ramp kinks on flow structures, unsteadiness and turbulence evolution, so the two ramp angles are kept unchanged.

Table 1
Geometric parameters for four DNS cases.

Case	L_f (mm)	L_c (mm)	L_d (mm)	L_y (mm)	L_z (mm)	α_1 (^{o})	α_2 (^{o})
DC1	400.0	6.0	43.0	33.8	14.0	12.0	24.0
DC2	400.0	12.0	37.0	33.8	14.0	12.0	24.0
DC3	400.0	18.0	31.0	33.8	14.0	12.0	24.0
DC4	400.0	24.0	25.0	33.8	14.0	12.0	24.0

The layout of this paper is organized as follows. In Section 2, the numerical methodology is briefly described, including flow configuration, computational setup, and incoming turbulent flow. The influence of the length between the two ramp kinks on SWTBLIs in a double compression ramp is analyzed and discussed in Section 3. Finally, conclusions are summarized in Section 4.

2. Direct numerical simulation

2.1. Flow configuration

Fig. 1(a) presents a sketch of the computational domain in the Cartesian coordinate (*x, y, z*) with the origin located at the corner of the first ramp, and a schematic view of the flat-plate/double compression ramp investigated is shown in Fig. 1(b). A zeropressure gradient turbulent boundary layer (TBL) spatially develops on a flat-plate and subsequently goes through a double compression ramp with $\alpha_1 = 12^o$ and $\alpha_2 = 24^o$. The streamwise extent (L_x) of the computational domain is composed of three regions, i.e., L_f, L_c, and L_d being the length of the flat-plate, the first ramp, and the second ramp, respectively. L_y and L_z denote the size of the computational domain in the wall-normal and spanwise directions, respectively. In this paper, four DNS cases are considered, which are denoted as DC1-DC4. Table 1 outlines the geometric parameters for all DNS cases. Note that the effects of L_c on the shock interactions are investigated by increasing L_c and keeping $L_c + L_d$ at a constant value of

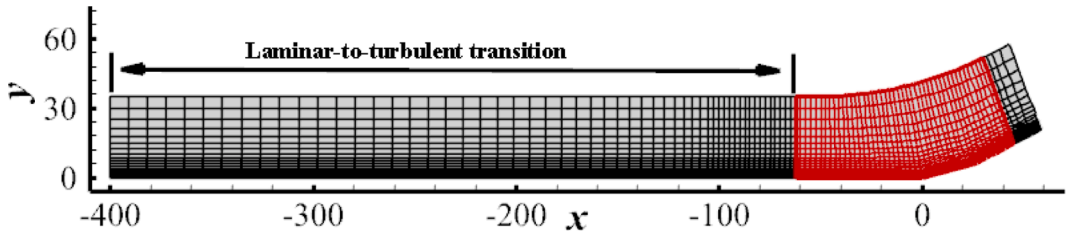

Fig. 2. Sketch of the computational grid. The grid is plotted at intervals of every ten and five points in both x and y directions, respectively.

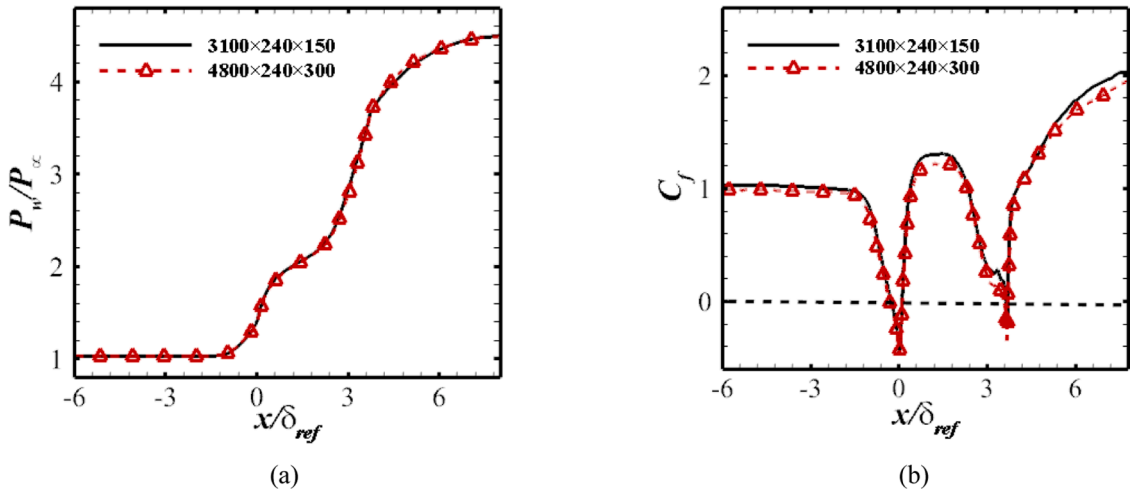

Fig. 3. Grid-sensitivity study for DC4: (a) mean wall pressure; (b) skin-friction coefficient normalized with the value at the reference plane.

49.0 mm. The inflow conditions are similar to DNS of Wu *et al.* [15]. The freestream Mach number $M_\infty = 2.9$, and the freestream temperate $T_\infty = 108.1K$. The Reynolds number based on the momentum thickness of TBL at $x = 60$ mm is $Re_\theta = 2253$.

2.2. Computational set-up

In our simulation, the open source high-order finite difference code, developed by Li *et al.* [21], is applied, which has been used with success to many DNS studies of turbulent flows [6],[19–20],[22–23]. The governing equations in curvilinear coordinates (ξ, η, ζ) are written as follows:

$$\frac{\partial U}{\partial t}+\frac{\partial(F+F_v)}{\partial \xi}+\frac{\partial(G+G_v)}{\partial \eta}+\frac{\partial(H+H_v)}{\partial \zeta}=0, \tag{1}$$

where U contains the conservative variables, F, G and H denote the convective flux terms in the ξ, η, and ζ directions, respectively. F_v, G_v and H_v denote the corresponding viscous flux terms. The working fluid is a perfect gas. The Sutherland's law is used to calculate the viscosity coefficient and the ideal-gas state equation is enforced. More details can be found in Tong *et al.* [22]. We utilize the WENO-SYMBO [24] scheme with a combination of absolute and relative limiters [15] and Steger-Warming splitting approach to discretize the inviscid terms, and use an eighth-order central difference scheme to calculate the viscous terms. The time advancement relies on the third-order explicit TVD Runge-Kutta method.

The computation grid is generated using analytical transformations, to ensure the grid orthogonally in the corner region. For all DNS cases, the mesh has 3100 × *240* × *150* grid points in the streamwise, wall-normal, and spanwise directions, respectively. As shown in Fig. 2, the grid points in the streamwise direction is partitioned into three zones: 1680 points in the transition zone ranging from $x = -400$ mm to $x = -60$ m, 1320 points uniformly distributed in the corner region, and 100 points in the fringe region extending from $x = 49$ mm to $x = 60$ mm with progressively coarsened spacing. In the wall-normal direction, 150 points are employed inside the boundary layer, and the grid points are hyperbolically stretched and clustered in the near-wall region to ensure sufficient accuracy. In the spanwise direction, the grid points are equally distributed. In wall units at the reference plane (see Fig. 4), the streamwise and spanwise grid spacing in the corner region are $\Delta x^+ = 3.6$ and $\Delta z^+ = 4.2$. The grid spacing at the first grid point above the wall and at the edge of the boundary layer are $\Delta y_w{}^+ = 0.4$ and $\Delta y_e{}^+ = 5.5$, comparable to those of previous well-accepted DNS data. Unless otherwise stated, δ_{ref} denotes the boundary layer thickness at x_{ref}, the subscript + represents the value under the inner scaling, the subscripts e and w denote the flow variables at the wall and boundary layer edge,

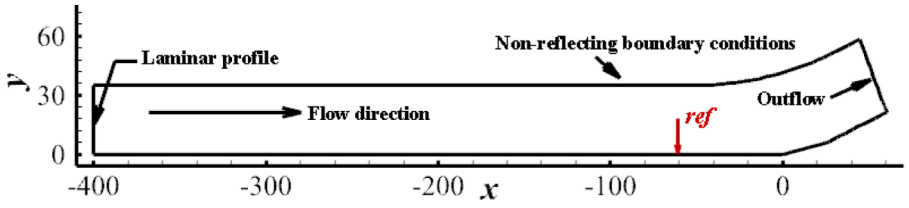

Fig. 4. Sketch of boundary conditions. The reference plane is taken at x= -60 mm, denoted as *ref*.

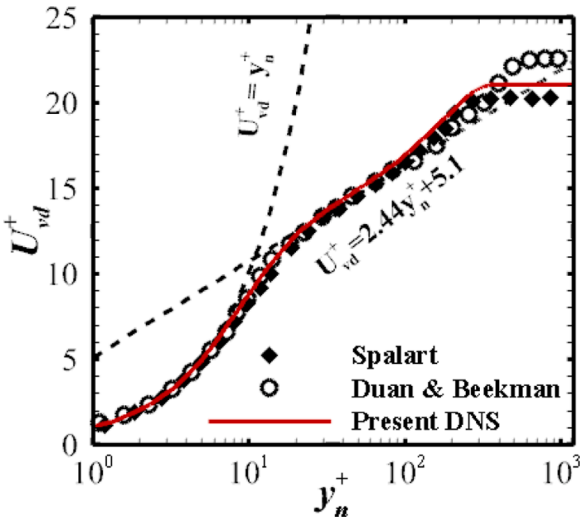

Fig. 5. Profile of the van Direst transformed mean velocity obtained at x_{ref}.

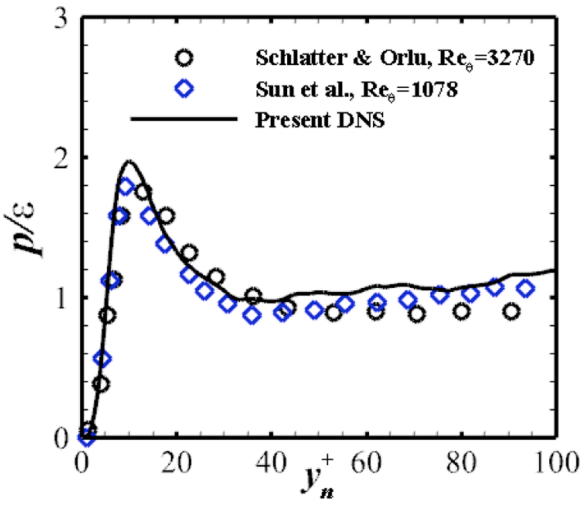

Fig. 7. Distribution of the production-to-dissipation ratio P/ε obtained at x_{ref}.

respectively. A grid-sensitivity study is further performed, where the grid in the interaction zone (remarked as red in Fig. 2) is refined by 100% in the streamwise and spanwise directions, respectively. It can be seen from Fig. 3 that the pressure distribution remains unchanged and the skin-friction is relatively insensitive to the grid resolution. The difference between the two grids is estimated to be less than 7% in the reattachment region, confirming that the current grid resolution is sufficiently fine.

The boundary conditions adopted in the simulation are sketched in Fig. 4. A steady laminar boundary layer profile is imposed at inlet. At outlet, outflow boundary conditions are enforced to eliminate the disturbance reflection, and the flow variables are obtained using the second-order downstream extrapolation. No-reflecting boundary conditions are used on the upper boundary. The selected domain width is sufficiently large to guarantee that the velocity correlation coefficients rapidly fall close to zero for large spanwise spacing, as reported in Fig. 4, and periodicity is utilized in the two spanwise boundaries. At the bottom wall, a no-slip boundary condition is applied with constant wall temperature $T_w = 307$ K. A laminar-to-turbulent transition method is used to generate the fully developed incoming TBL over the flat-plate, as was used by Pirozzoli *et al.* [25]. A tripping region of blowing and suction velocities covers the region -370 mm $< x <$ -350 mm and $0 < z < 14$ mm at the wall. For all interactions, the incoming TBL is fully developed at the reference plane (x_{ref}), which will be further validated in the following section.

To guarantee statistical convergence, the mean and statistical properties in the present study are computed using 600 three-dimensional instantaneous flow fields, with a constant sampling time of $\Delta t U_\infty/\delta_{ref} \approx 1.54$. The wall pressure signals along the streamwise direction are periodically sampled at a shorter time interval of $\Delta t U_\infty/\delta_{ref} \approx 0.07$ to accurately resolve the unsteadiness in STBLIs. In the following analysis, the mean refers to the average in time and the spanwise direction, the generic variable φ is decomposed using the Reynolds average ($\varphi = \overline{\varphi} + \varphi'$) or the density-weighted average ($\varphi = \widetilde{\varphi} + \varphi''$ and $\widetilde{\varphi} = \overline{\rho\varphi}/\overline{\rho}$).

2.3. Characteristics of incoming TBL

To validate the incoming TBL, we quantitatively compare the computed results at x_{ref} and those of a canonical zero pressure gradient flat-plate TBL, including mean velocity profile, turbulence intensities, and production-to-dissipation ratio.

In Fig. 5, the van Driest transformed mean velocity profile at x_{ref} is compared with the incompressible DNS data of Spalart [26] and supersonic numerical results of Duan and Beekman [27], showing a reasonable agreement. The main difference is observed in the wake region, because of the different Reynolds number selected. Clearly, the law

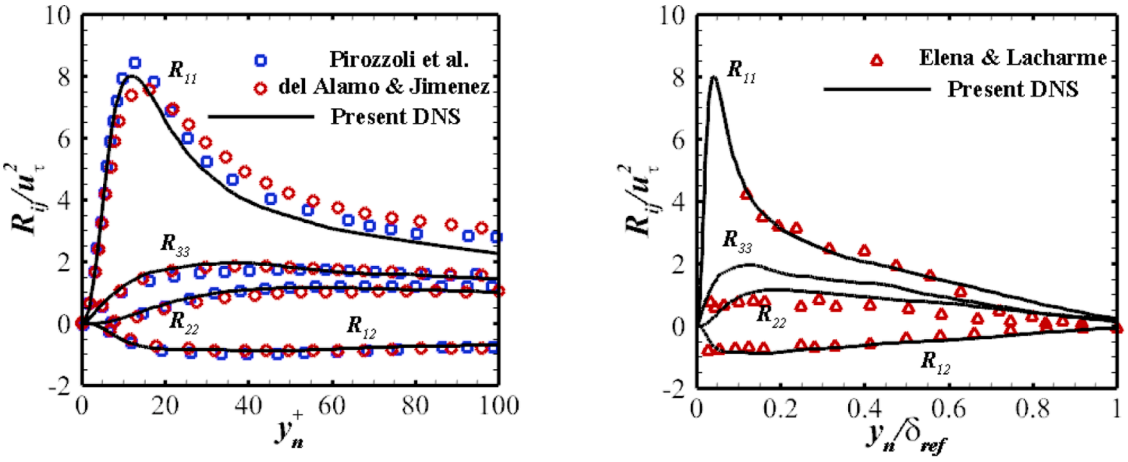

(a) (b)

Fig. 6. Profiles of the density-scaled Reynolds stress components $R_{ij} = (\overline{\rho}/\overline{\rho}_w)\widetilde{u''_i u''_j}$ at x_{ref}: (a) inner scaling; (b) outer scaling. The results are scaled with the square of friction velocity u_τ at x_{ref}.

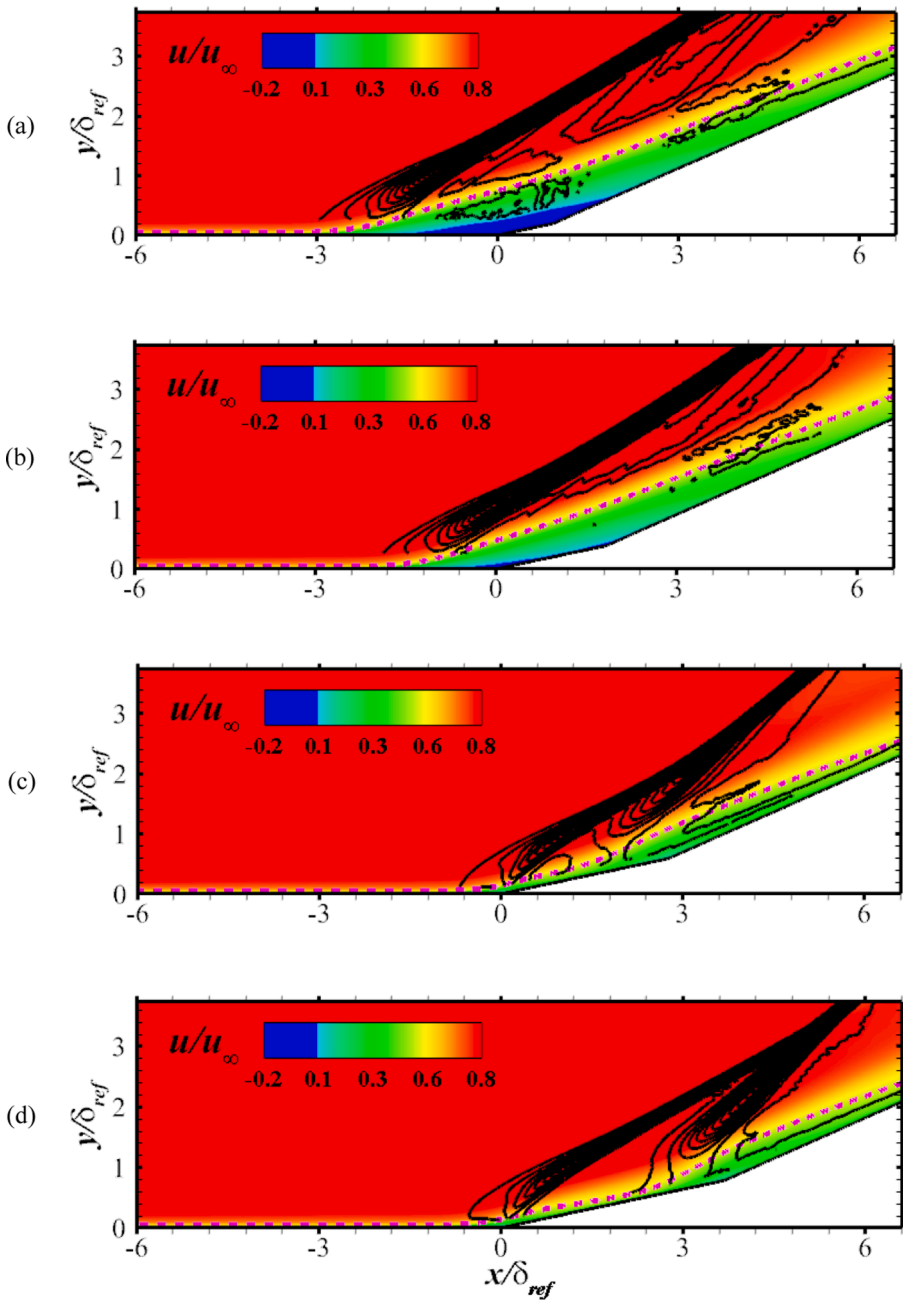

Fig. 8. Contours of mean streamwise velocity and iso-contours of pressure gradient with fifty levels from 0 to 16.25: (a) DC1; (b) DC2; (c) DC3; (b) DC4. The dashed line denotes the mean sonic line.

of the wall is observed in the linear sub-layer $y^+_n < 10$, with a narrow region characterized by the log low for $30 < y^+_n < 90$. Note that y_n denotes the wall-normal distance, hereafter. The density-scaled Reynolds stress components presented with the inner and outer scaling are shown in Fig. 6, respectively, together with the incompressible DNS of channel flow by del Alamo & Jimenez [28], supersonic experimental data of Elena & Lacharme [29], and DNS data of Pirozzoli *et al.* [30] at Mach 2. It is clear that the computed results in the near-wall region and outer part of the incoming TBL match well with previous experimental and numerical data, supporting the Morkovin's compressible scaling. Moreover, Fig. 7 shows the production-to-dissipation ratio (P/ε) distribution to check the local equilibrium in the log layer of the incoming TBL, where the incompressible boundary layer DNS data of Schlatter and Örlü [31] at $Re_\theta = 3270$ and compressible DNS data of Sun *et al.* [32] at $Re_\theta = 1078$ are also included for comparison. The production and dissipation of the turbulence kinetic energy are defined as

$$P = -\overline{\rho}\widetilde{u''_i u''_j}\frac{\partial \widetilde{u''_i}}{\partial x_j}$$

$$\varepsilon = \overline{\sigma'_{ij}\frac{\partial u''_i}{\partial x_j}}, \tag{2}$$

with σ_{ij} being the viscous stress tensor. As expected, the ratio increases, attains a maximum value of $P/\varepsilon = 2$ at $y^+_n \approx 10$, and then rapidly drops, approaching to unity in the logarithmic region, suggesting that the local equilibrium is fully completed.

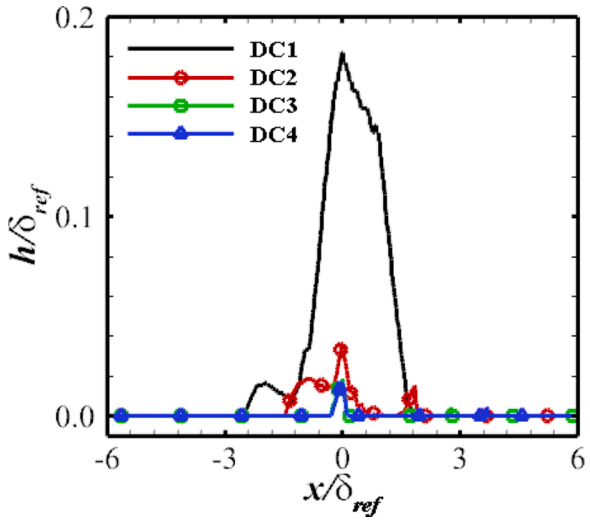

Fig. 9. Distribution of mean separation bubble height.

3. Results and discussion

3.1. Mean properties

Fig. 8 shows contours of mean streamwise velocity field, superimposed with iso-contour lines of pressure gradient and mean sonic lines in pink dashed lines. As expected, increasing L_c exhibits significant influence on the mean properties. The extent of the separation region significantly decreases and the sonic line gradually approaches towards the wall, resulting in smaller irregular subsonic region. In particular, no considerable reversed flow is observed in DC3 and DC4. Another notable difference is the significant variations of the shock wave system determined by the pressure gradient. Clearly, the shock patterns in DC1 and DC2 are similar to those observed in compression ramp interactions by Wu *et al.* [15]. However, as L_c is further increased, the entire shock wave system moves downstream, corresponding to the reduced separation region, and the interactions are mainly characterized by a λ-shock-wave system, with the front leg being formed near the first corner and the rearward stem originating above the second corner. For DC4, the front shock wave is slightly changed, while the rear shock wave seems to be strengthened and bent significantly. Meanwhile, the major influence of L_c is also apparent from the bubble height, determined by the wall-normal location of the zero streamwise velocity iso-line. Fig. 9 shows that the bubble mass mainly concentrates in the downstream portion of the reversed flow and is mostly affected by increasing L_c. For DC1 and DC2, the upstream portion of the bubble keeps a near-constant height of $0.02\delta_{ref}$. Increasing L_c significantly reduces the bubble height in the downstream portion. For DC2-DC4, the height of the first bubble drops to approximately 9% - 18% of DC1 and the recirculating flow in the second bubble is negligible. It is believed that the effect of increasing L_c exhibits significant influence on the bubble height.

Fig. 10. shows the development of the boundary layer properties across the interaction region for all cases, where the compressible displacement thickness and momentum thickness are defined as

$$\delta^* = \int_0^{\delta_e} (1 - (\rho / \rho_e)(u / U_e))dy_n,$$

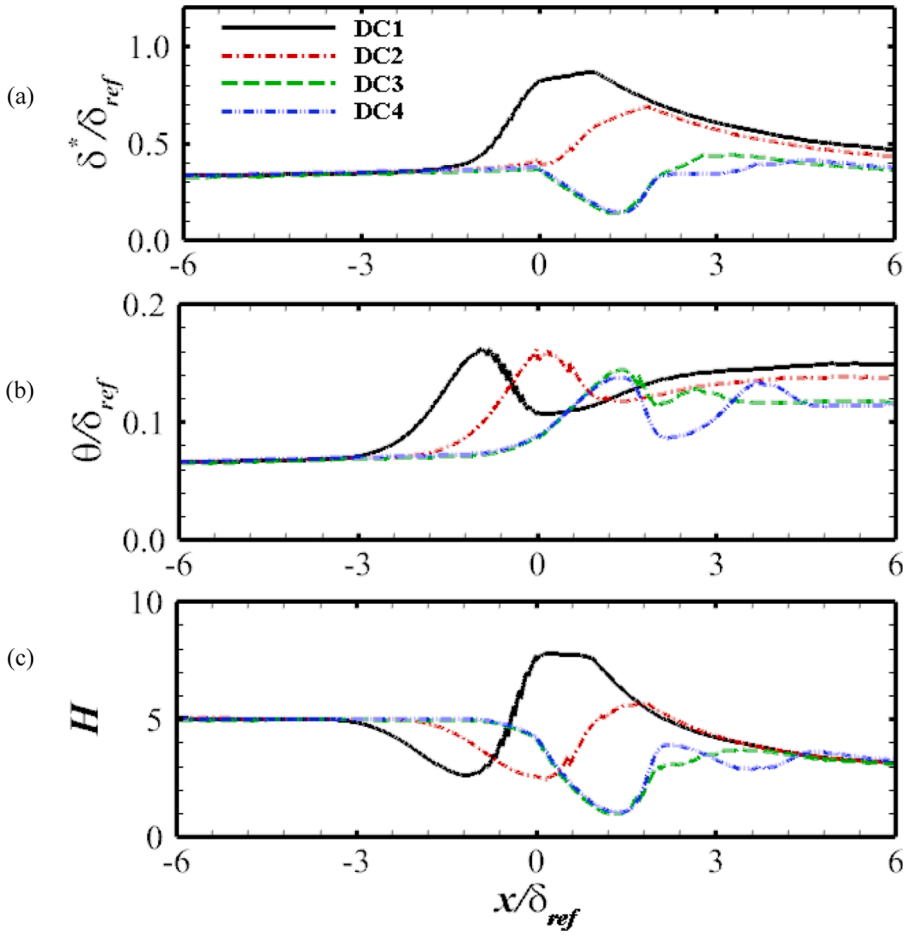

Fig. 10. Streawise evolution of boundary layer properties for the (a) displacement thickness δ^*, (b) momentum thickness θ and (c) shape factor H.

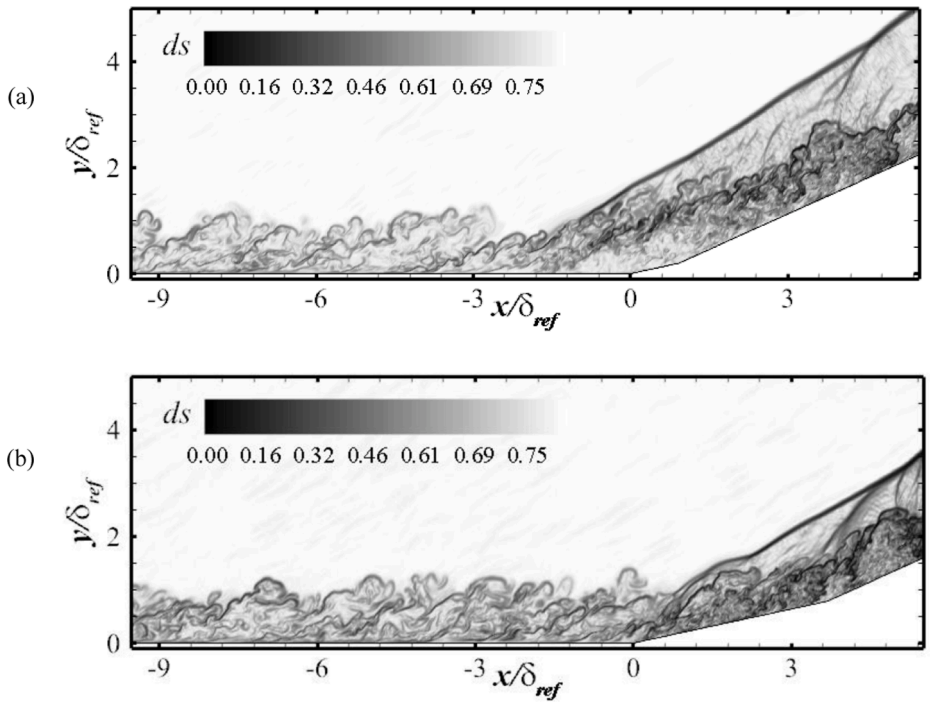

Fig. 11. Contours of instantaneous density gradient in an *x*-*y* plane: (a) DC1; (b) DC4.

$$\theta = \int_0^{\delta_e} (\rho/\rho_e)(u/U_e)(1-(u/U_e))dy_n, \tag{3}$$

with U_e and ρ_e being the mean velocity and density at the boundary layer edge (δ_e), respectively. Instead of the percentage 99% (δ_{99}) commonly used in canonical flow, the method introduced by Pirozzoli *et al.* [33] and Garnier *et al.* [34] is adopted to estimate δ_e, which is physically defined at the wall-normal distance where ω_z becomes less than a threshold. Assuming that ω_z remains theoretically unchanged in the upper inviscid regime across the interaction, a threshold of $0.005U_\infty/\delta_{ref}$ is selected which makes δ_e coincide with the traditional δ_{99} in the upstream TBL. Along the surfaces of DC1 and DC2, δ^* experiences a considerable rise due to the development of the separation bubble, followed by a gradual reduction in the recovery process, while the displacement thickness in DC3 and DC4 first decreases at $x/\delta_{ref} \approx 0$, attaining a minimum value of $\delta^*/\delta_{ref} = 0.14$ at $x/\delta_{ref} \approx 1.4$, then exhibits a slow increase further downstream. As shown in Fig. 10(b), the momentum thickness is characterized by similar behavior, where it increases slowly from the value of the upstream TBL and drops rapidly before re-growing in the downstream region. Profiles for DC3 and DC4 collapse at $x/\delta_{ref} > 4.2$, having lower value than those of DC1 and DC2. Fig. 10(c) shows the distributions of the compressible shape factor, defined as $H=\delta^*/\theta$. Upstream the interaction, a good collapse of the profiles is observed at $x/\delta_{ref} < 3.0$. In the present study, the computed result is $H = 4.97$, just falling in the theoretical range of [4.47, 5.03] predicted by Monaghan [38] in the case of zero pressure gradient compressible TBL. It can be seen that the distribution is consistently characterized by two local extrema for all interactions, but differences between them become less significant with increasing L_c. Downstream of the interaction, it undergoes a decline process and collapses at $x/\delta_{ref} > 4.2$, attaining an approximate value of about 3.2, much lower than that of the upstream TBL.

3.2. Turbulent structure

To gain insight into flow structures, we further compare the results from DC1 and DC4. Snapshots of the instantaneous density gradient in an *x*-*y* plane are given in Fig. 11, which is defined as [15]

$$ds = 0.8\exp\left[-10\left(|\nabla\rho| - |\nabla\rho|_{\min}\right) / \left(|\nabla\rho|_{\max} - |\nabla\rho|_{\min}\right)\right]. \tag{4}$$

Apparently, the main shock and fine structures inside the TBL are both well resolved. The instantaneous results also highlight a significant augmentation of turbulence. After passing through the shock, the outer region of the boundary layer becomes steeper and more convoluted than those of the incoming TBL. A few shocklets are also observed at the reattachment boundary layer edge due to strong compression. In Fig. 12, the three-dimensional instantaneous vortical structures are extracted with an isosurface of the *Q* criterion [35] coloured by the wall-normal distance and the black isosuface of streamwise velocity $u = 0$ is used to display the reversed flow. For better comparisons, a relatively high threshold of Q/Q_{max}= 0.05 is used to reduce the number of detected vortical structures, with attentions only being paid on the vortex evolution inside the interaction. As expected, few vortical structures are observed in the upstream TBL, while the captured vortical structures for both cases are strongly three-dimensional. In agreement with the findings of Priebe *et al.* [17], the result in Fig. 12(a) reveals that large-scale streamwise vortical structures are significantly formed at separation and subsequently lifted-off wavy from the wall, leading to the onset of larger coherent vortices in the outer region of the reattachment boundary layer. Qualitative comparisons between DC1 and DC4 demonstrate that increasing L_c gives lower vortex production, where the vortical structures become sparse and much smaller due to weak interaction. Since the separation bubble becomes much smaller and decomposes into two isolated parts, thus the vortices gets closer to the wall, only predominant in the near-wall region.

In Fig. 13, the contour maps of time-averaged vorticity ω^* as well as streamlines on a slice at $x/\delta_{ref} = 6.0$ are reported. Note that ω^* is the transformed dimensionless vorticity in the direction parallel to the ramp surface, which is expressed as

$$\begin{aligned} \omega^* &= \omega_x \cos 24^o + \omega_y \sin 24^o, \\ \omega_x &= (\partial w/\partial y - \partial v/\partial z)\delta_{ref}/U_\infty, \\ \omega_y &= (\partial u/\partial z - \partial w/\partial x)\delta_{ref}/U_\infty. \end{aligned} \tag{5}$$

Here, ω_x and ω_y denote the corresponding streamwise and normal components of vorticity vector in Cartesian coordinates (*x*, *y*, *z*). Also

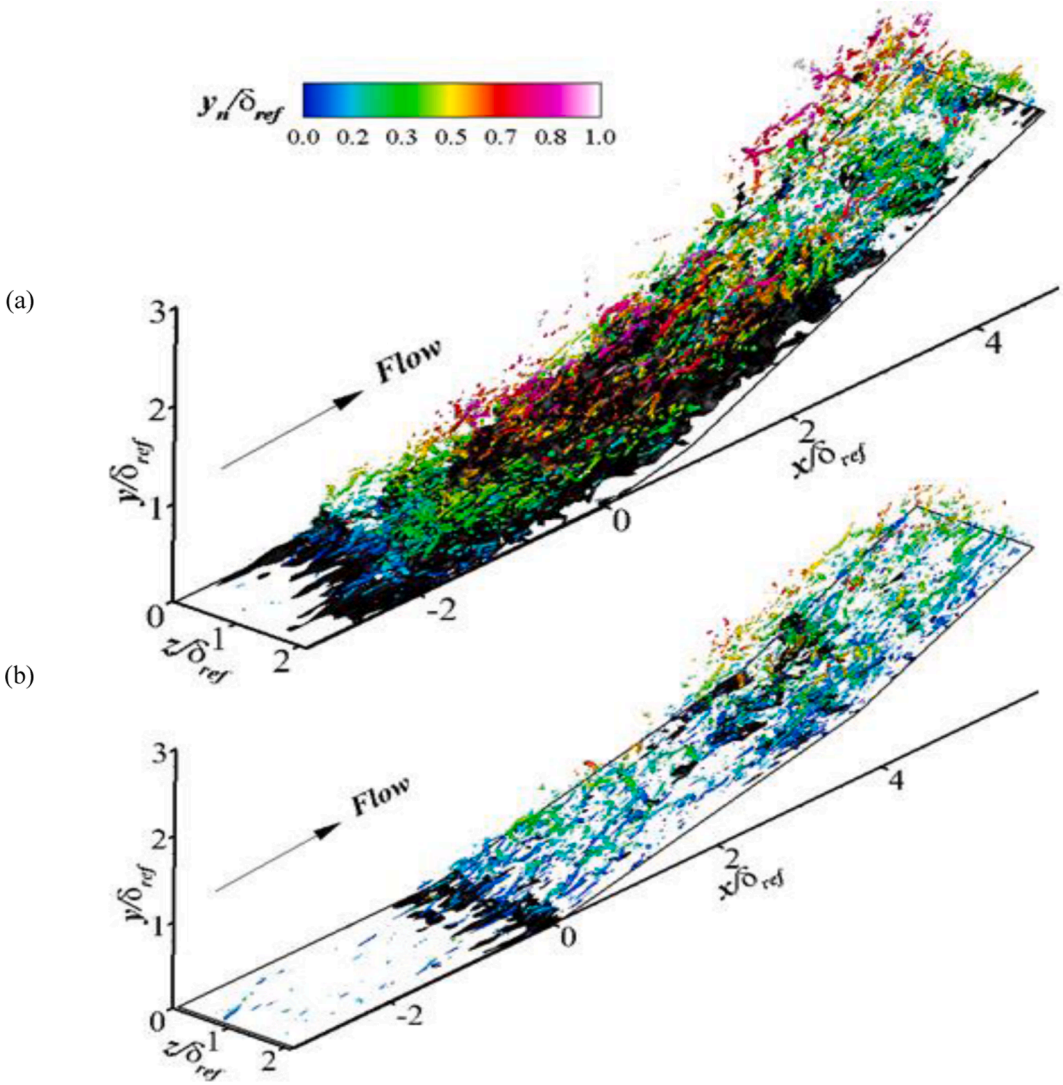

Fig. 12. Isosurface of the Q criterion (Q/Q_{max}=0.05) coloured by the wall-normal distance y_n: (a) DC1; (b) DC4. Isosurface of streamwise velocity $u = 0$ is reported in black.

shown is the wall-normal location of the boundary layer edge, denoted by the white dash line. To display the presence of Görtler-like vortices, following Dawson & Lele [36], the streamlines are determined by the perturbation velocities in the direction perpendicular to the wall and in the spanwise direction, and the time-spanwise averaged values are subtracted. In previous experimental studies of STBLIs in a 24° compression ramp, Settles *et al.* [3] conjectured that the spanwise variation of the separation length was attributed to the formation of Görtler-like vortices in the interaction due to the concave streamline curvature. As pointed by Loginov *et al.* [37] and Grilli *et al.* [38], the spanwise width of the Görtler-like vortex pairs in their LES of a 25^0 compression ramp interaction was approximately $2\delta_0$, with δ_0 being the thickness of the incoming TBL. The present results highlight that intense localized regions of positive and negative vortex are generated within the downstream TBL and alternatively located in the spanwise direction, further supporting the existence of the steady counter-rotating streamwise vortices. Correspondingly, the streamlines significantly swirl and large-scale roll cells are formed in the spanwise direction, which is an indicator of the up-wash of lower momentum fluids and the down-wash of higher momentum fluids. Due to the background turbulence, these regions are mostly characterized by frequently scattered spots, exhibiting a strong intermittent behavior. We observe that the flow patterns in DC1 are very similar to those of previous compression ramp interaction. The spanwise width of the large-scale roll cells seems to be nearly unchanged and attains an approximate value of δ_{ref}. Moreover, the core of these roll cells is approximately located at $y_n/\delta_{ref} = 0.5$, also in agreement with the results of Dawson & Lele [36]. It is suggested that the effect of small L_c on the streamwise vortices is negligible. By contrast, two dominant trends with increasing L_c can be made from Fig. 13(b): (i) the spanwise width of the localized regions with negative and positive values dramatically decreases and (ii) the spatial distribution of the roll cells becomes more regular.

Considering the computational domain of $L_z = 2.2\delta_{ref}$ and periodic boundary conditions used in our simulation, the spanwise wavelength of the streamwise vortices drops to be nearly $0.5\delta_{ref}$, leading to four large-scale roll cells to be captured in the spanwise direction. The effect of larger L_c on the characteristics of the large roll cells is further quantitatively supported by probability density functions (PDFs) of the streamwise vortex at two wall-normal locations, as reported in Fig. 14. One probe is located in the inner wall region at $y_n/\delta_{ref} = 0.04$ and the other is inside the large roll cells at $y_n/\delta_{ref} = 0.71$. Obviously, all PDFs in both cases display a nearly symmetric distribution. As expected, the PDFs at $y_n/\delta_{ref} = 0.04$ collapse well, suggesting weak dependence of increasing L_c in the near-wall region. However, at $y_n/\delta_{ref} = 0.71$, the profile for DC4 shows higher peak and the PDF tail becomes narrow, compared to that of DC1. It is confirmed that increasing L_c tends to

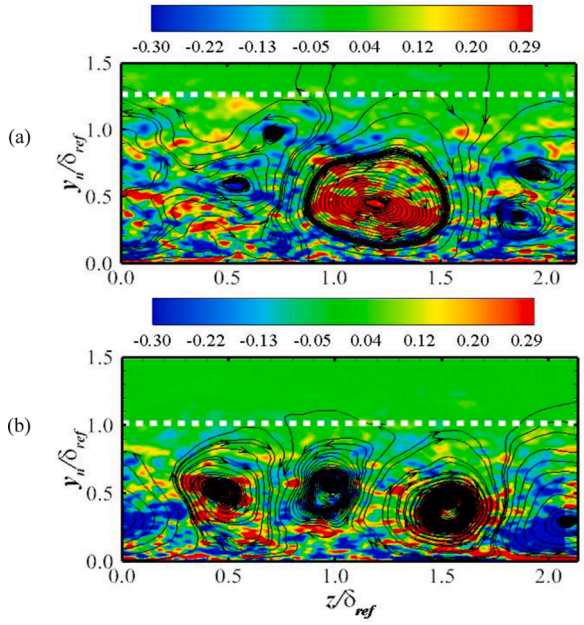

Fig. 13. Contours of time-averaged streamwise vorticity ω_x^* and streamtraces in two spanwise/wall-normal planes: (a) DC1; (b) DC4. The white dashed lines denote the boundary layer thickness.

increase the occurrence probability of events with smaller streamwise vorticity.

The decreased spanwise width and the regularization of the counter-rotating streamwise vortices associated with increasing L_c can be explained from the distribution of the curvature parameter δ/R and the Görtler number G_T, reported in Fig. 15. As suggested by Simit & Dussauge [39], the Görtler number G_T, defined as

$$G_T = \frac{(\theta/\delta)^{3/2}}{0.018(\delta^*/\delta)}\sqrt{\frac{\delta}{R}}. \tag{6}$$

can be used to estimate the generation of the Görtler vortices in the compressible turbulent separated flow. Here, the curvature parameter δ/R is defined as the ratio of the boundary layer thickness δ to the curvature radius of the streamline, given as [40]

$$R = \frac{(u^2+v^2)^{3/2}}{\left(u^2\frac{\partial v}{\partial x} - v^2\frac{\partial u}{\partial y} + uv\left(\frac{\partial v}{\partial y} - \frac{\partial u}{\partial x}\right)\right)}. \tag{7}$$

In Fig. 15, we compare the distribution of δ/R and G_T along the streamline staring at $(x, y) = (-6.0\delta_{ref}, 0.5\delta_{ref})$ for DC1 and DC4. Consistent with Priebe *et al.* [18], δ/R and G_T in both cases have a peak value near the separation point, much higher than the critical value of $\delta/R = 0.03$ given Simit & Dussauge [40] in Mach 3 flow and $G_T = 0.6$ given by Loginov *et al.* [37] in laminar flow. Although the critical value for the turbulent flow has not yet been determined, it is reasonable to conjecture that the Görtler-like mechanisms related with the centrifugal instability might be the likely explanation for the observed streamwise vortices in our simulation. Clearly, the peak value increases as L_c increases. It is interesting to note that a local maximum of δ/R and G_T appears in the downstream region of DC4 at $x/\delta_{ref} = 3.0$, just before the streamwise location of the second ramp, where δ/R and G_T for DC1 are just close to the critical value. It seems like that the streamwise vortices are more likely to form in the case of larger L_c. This phenomenon can be understood from the following two aspects. First, increasing L_c decreases the separation bubble size in the first ramp, leading to a significant increase of the streamline curvature at separation. Second, the presence of the second ramp acts like an enhancer to promote the activities of the generated Görtler-like vortices and theirs resistance to back turbulence as these vortices develop downstream.

3.3. Wall pressure and skin-friction

In Fig. 16, we focus on the effect of increasing L_c on the distributions of mean wall pressure. Due to the strong compression, the wall pressure increases consistently for all cases, but streamwise variations of the wall pressure are utterly different. For DC1 and DC2, increasing L_c only produces a downstream shift of the initial pressure rise and a reduction of the pressure-plateau, associated with the shrinkage of the separation bubble, while a good collapse is clearly identified for $x/\delta_{ref} > 1.0$. A different behavior occurs for DC3 and DC4. We observe that the pressure experiences a slight increase after passing the front shock wave and both curves exhibit good collapse for $x/\delta_{ref} < 0.6$, indicating insensitivity of the second ramp on the interaction in the first ramp. It is worth noticing that all the curves matches very well for $x/\delta_{ref} > 6.0$ and gradually approach the theoretical prediction obtained from the Rankine-Hugoniot jump conditions, suggesting that the total adverse pressure gradient throughout the interaction is independent of L_c.

Fig. 17 shows the weighted power spectral density (PSD) of wall pressure signals at mean separation point x_{sep} for all cases to provide information about the unsteadiness of shock motion in STBLIs. Here, the weight PSD is calculated using the method given by Pasquariello *et al.* [41], which is defined as $f\cdot\Phi(f)/\int\Phi(f)df$ with f and Φ being the frequency and PSD, respectively. In Fig. 17, the weight PSDs of wall pressure fluctuations normalized with its maximum value is reported as

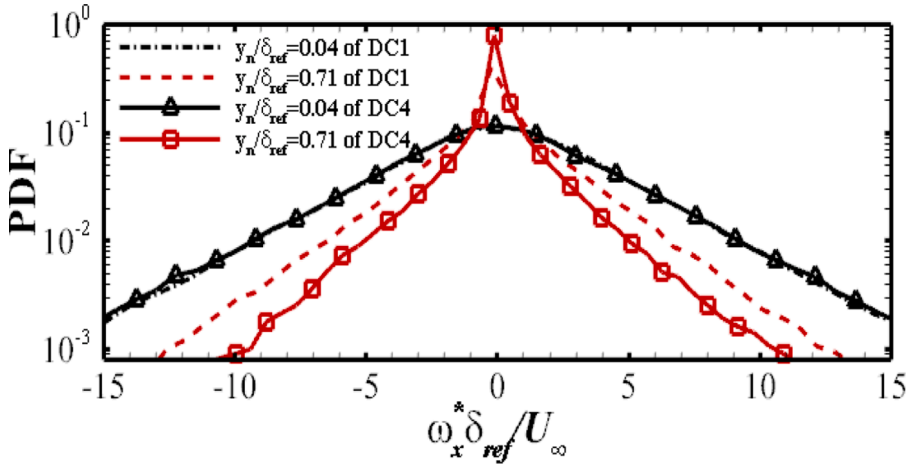

Fig. 14. Probability density functions of the transformed streamwise vorticity at two wall-normal locations for DC1 and DC4. The DNS data is taken at $x/\delta_{ref} = 6.0$.

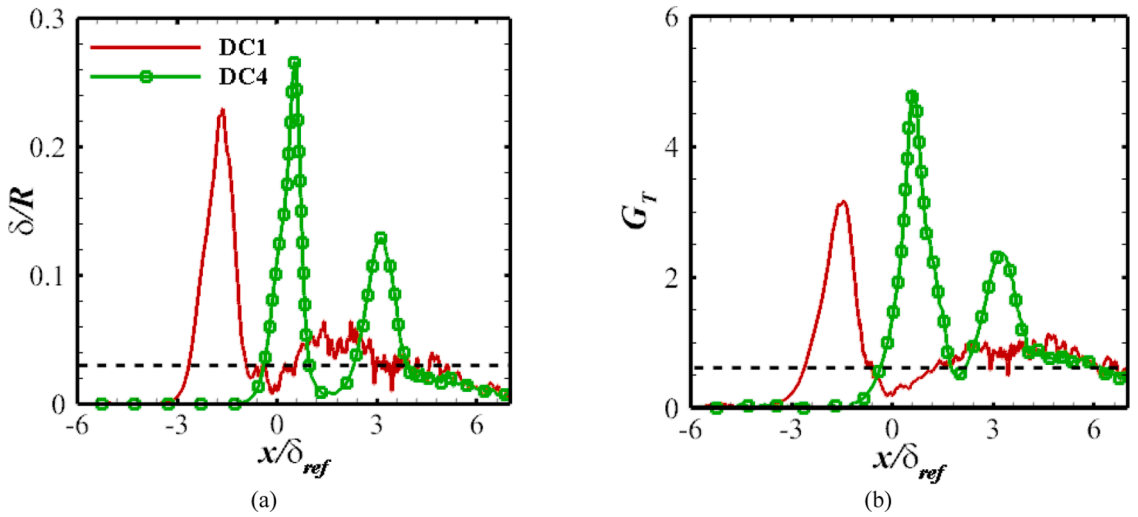

Fig. 15. Distributions of (a) streamline curvature and (b) Görtler number along the mean streamline passing through $x = -6.0\delta_{ref}$ and $y = 0.5\delta_{ref}$.

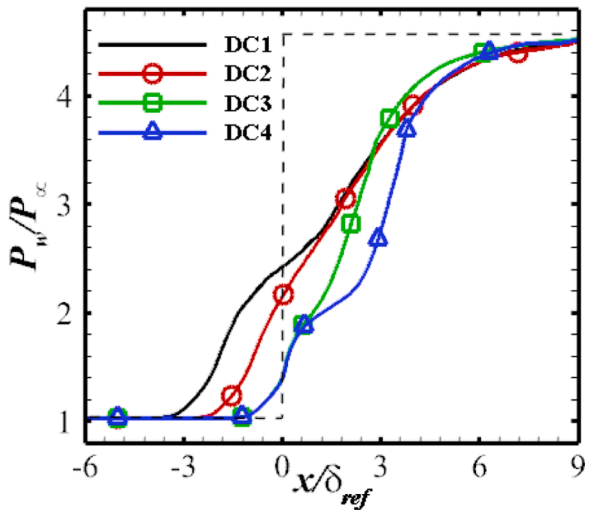

Fig. 16. Distribution of mean wall pressure with the inviscid distribution for 24° compression ramp in dashed black line.

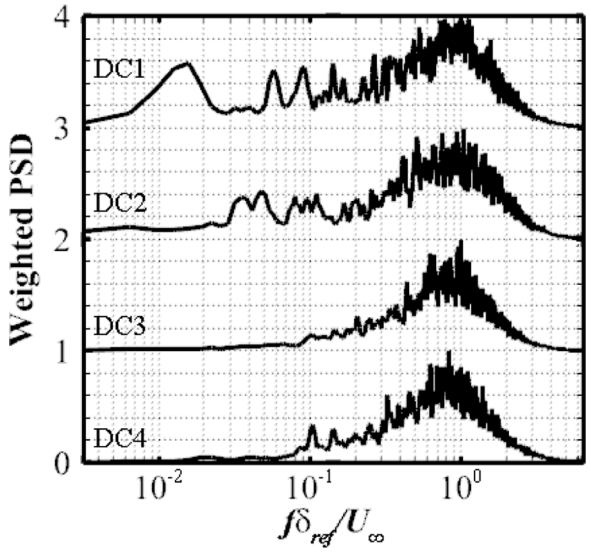

Fig. 17. Weight power spectral density of wall pressure fluctuation at mean separation point x_{sep}. Each profile is normalized by its maximum and shifted upstream along the vertical axis.

a function of non-dimensional frequency $f\delta_{ref}/U_\infty$. We can see that the spectra are strongly affected by increasing L_c, particularly the low-frequency content. Although the dominant non-dimensional frequency $f\delta_{ref}/U_\infty$ shifts to higher frequencies, the spectra for DC1 are still characterized by low-frequency peaks, suggesting that the low-frequency shock motion is evident. Such behavior is completely changed for DC2-DC4, where an increase of L_c results in a significant reduction of low-frequency energy, and the broadband peak around $f\delta_{ref}/U_\infty \approx 1.0$ is insensitive to L_c. This leads to most part of energy concentrated at high-frequency content, implying that the shock motion is only dominated by high-frequency unsteadiness. The differences might be a direct consequence of the dramatically decreased bubble mass, provided that the low-frequency unsteadiness originates from the downstream separated flow. For DC1, the separation length and bubble height are much larger, compared to those of the other three cases. For interactions with weak separation (DC3 and DC4), the contributions from the high-frequency fluctuations in the upstream TBL are expected to become significant, resulting in the suppression of the low-frequency shock unsteady motion.

Profiles of mean skin-friction along the surface of the double compression ramp are depicted in Fig. 18. A good collapse is observed upstream the interaction and it drops rapidly close to the interaction. For all cases, the separation bubble is identified, where L_{sep} decreases with increasing L_c, consistent with qualitative behavior seen in Fig. 8. For DC1 and DC2, the skin-friction in the separation region is characterized by a typical *W*-shape with two local minima, also found in the DNS of oblique shock wave/turbulent boundary layer interactions conducted by Bernardini *et al.* [42]. An increase of L_c produces a significant downstream movement of the separation point x_{sep}, while the location of the reattachment point x_{ret} is less influenced, only being shifted downstream slightly. Nevertheless, the distribution of the skin-friction seems to be insensitive to L_c and substantially obeys the above *W*-shape. For DC3 and DC4, the separation is mainly dominated by two smaller isolated regimes, with the size of about $0.5\delta_{ref}$ and $0.2\delta_{ref}$, respectively. Based on the plateau region with positive values in the region of $0 < x/\delta_{ref} < 3.0$, it is reasonably inferred that there are considerable attached flow re-appeared between them. Moreover, increasing L_c exhibits little effect on the separation region size in the latter two cases, except for the location of the second separation for DC4 moving further downstream.

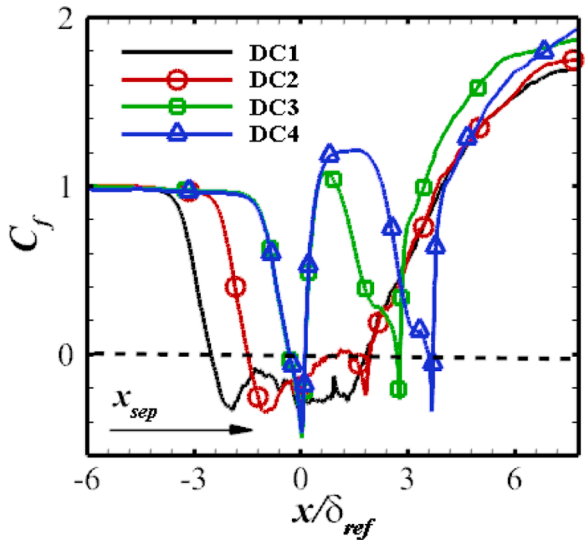

Fig. 18. Distribution of mean skin-friction normalized with the value at x_{ref}.

3.4. Turbulence statistics

To reveal the effect of increasing L_c on turbulence evolution, we further discuss turbulence statistics in terms of Reynolds stress tensor components, turbulent kinetic energy, and anisotropy invariant map, at five streamwise locations. Here, the first station E_1 is at the reference point x_{ref}. The second to fourth points, corresponding to the first corner, middle point of the two corners, and the second corner, are referred as E_2, E_3, and E_4, respectively. The fifth point is at $x/\delta_{ref} = 6.0$, denoted as E_5. The relative positions of the sampling lines for DC1 are illustrated in Fig. 19. In the following analysis, the transformed velocity fluctuations (u_s'' and v_n'') are in the directions parallel and normal to the ramp surface, which are obtained by

$$u_s'' = u''\cos\alpha + v''\sin\alpha,$$

$$v_n'' = -u''\sin\alpha + v''\cos\alpha, \tag{8}$$

with α, u'', and v'' being the local turning angle of the ramp, the velocity fluctuations in the directions x and y, respectively.

In Fig. 20, we compare the Reynolds stress components $\tau_{11} = \overline{\rho u_s'' u_s''}$, $\tau_{12} = \overline{\rho u_s'' v_n''}$ and $\tau_{22} = \overline{\rho v_n'' v_n''}$ at four locations E_2-E_5, respectively. The results at location E_1 are also included for a reference purpose. In general, profiles of the computed Reynolds stress components exhibits qualitative similarities with previous findings of Adams [14] and Loginov *et al.* [37] in compression ramp interactions. Across the interaction zone, the maximum value is significantly increased, indicating strong turbulence amplification. Also, the peak location is shifted away from the ramp surface, which is related with the formation of the detached shear layer and the development of the separation bubble. The behaviors become more significant as L_c is increased. This can be attributed to the combined effect of the suppressed separation region and the increased streamwise distance between the selected four locations. Some interesting features can be made. First, it can be seen from Fig. 20(b) that profiles of τ_{11} for DC3 and DC4 are characterized by a double-peaked distribution, with one peak in the inner region and the other in the outer region. Differently, the Reynolds normal stress for DC1 and DC2 is dominated by a single outer peak. Recalling the skin-friction distribution shown in Fig. 18, no separation is observed at location E_3 in the latter two cases, while the flow at this location are strongly separated in the former two cases. Similar to the analysis of Fang *et al.* [43], it is inferred that the inner peak is related with the newly regenerated near-wall turbulence downstream of the first interaction with the front shock wave, and the outer peak is associated with the enhanced upstream turbulence, predominant in the outer region of the reattachment boundary layer. Similarly, the results in Fig. 20(d) also exhibit a double-peaked behavior for all interactions, in which the outer peak plays the leading role. Second, from Fig. 20(d, h, l), it is worth noticing that the Reynolds stress components (others not shown for space limitation) at location E_5 are found to collapse well in the region of $y_n/\delta_{ref} < 0.5$, implying that the near-wall turbulence downstream of the second interaction is insensitive to L_c. Nevertheless, the changes are clearly presented in the outer region, where the peak value slightly decreases and its location moves inward as L_c is increased.

Fig. 21 compares the profiles of turbulence kinetic energy (TKE), defined as $= \widetilde{u_i'' u_i''}/2$, at various streamwise locations for all cases. Compared to the upstream level, the TKE is remarkably amplified throughout the interaction. Notably, the effect of L_c on turbulence amplification can be understood with two different evolution processes. For DC1 and DC2, turbulence at location E_2 has shown significant amplification, and the maximum value appears in the outer region. This is related to energetic structures in the detached shear layer. Further downstream at locations E_3 and E_4, the turbulence enhancement in the outer region becomes more pronounced due to the rapid development of the shear layer, similar to previous observations in supersonic compression ramp [37–38]. In contrast, significant differences are to be noted as L_c is further increased. At location E_2, the TKE profiles for DC3 and DC4 match very well. Importantly, the smaller peak is located much closer to the wall because of the dramatically reduced separation region, and little changes are observed in the outer layer, where a good collapse is found at $y_n/\delta_{ref} > 0.5$. At location E_3, as the reattached boundary layer keeps growing, the peak value undergoes a considerable reduction and is approximately constant for $0.1 < y_n/\delta_{ref} < 0.3$, which is remarkable for DC4. In the outer layer, the TKE profiles seem to be slightly changed. At location E4, a pronounced increase emerges again in the near-wall region and the TKE in the outer layer is seen to be strengthened, which can

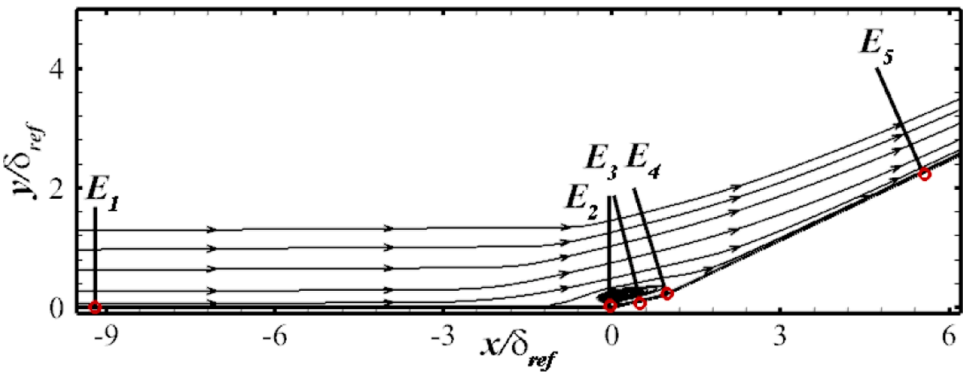

Fig. 19. Sketch of mean streamlines and sampling lines for DC1.

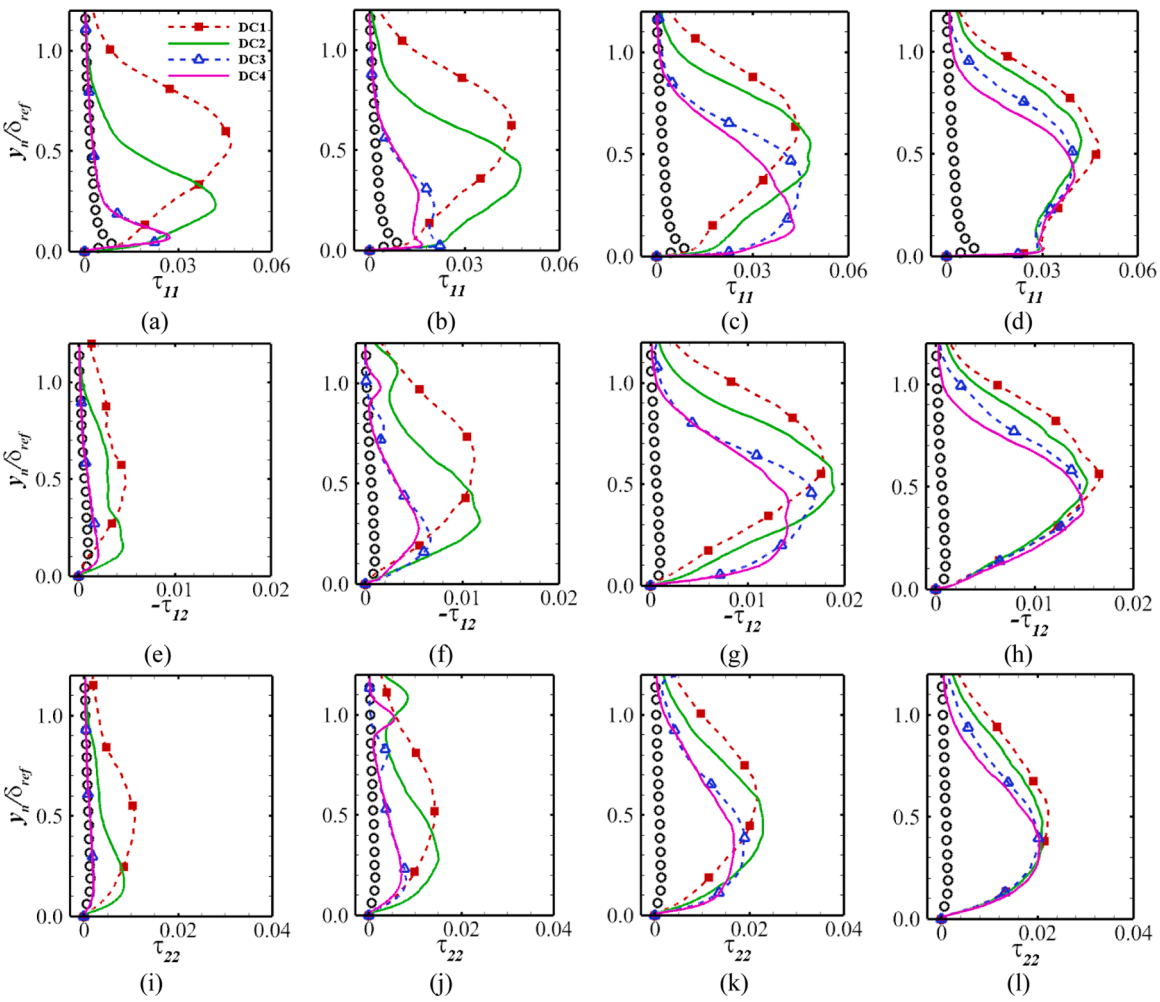

Fig. 20. Distributions of the Reynolds stress components at various streamwise locations: (a, e, i) E_2; (b, f, j) E_3; (c, g, k) E_4; (d, h, l) E_5. Open circles refer to the results taken at E_1.

be attributed to the interaction with the rear leg of the λ-shock-wave system. Despite the amplification mechanisms are different across the interaction, the TKE profiles downstream of the interaction are characterized by similar behavior, as reported in Fig. 21(d). Similar to profiles of Reynolds stress components in Fig. 20(d, h, l), the results in the near-wall region match very well, while the TKE in the outer layer is strongly affected, an increment of L_c implying an inward movement of the profile.

As suggested by Lumley [44], the different amplification of the Reynolds stress components can be examined using the invariants of the Reynolds stress anisotropy tensor b_{ij}, written as $b_{ij} = \widetilde{u_i'' u_j''}/2K - \frac{1}{3}\delta_{ij}$. By using the second II_b and third III_b invariants of b_{ij}, defined as $II_b = -\frac{1}{2}b_{ij}b_{ji}$ and $III_b = \frac{1}{3}b_{ij}b_{jk}b_{ki}$, they have proposed an anisotropy invariant map, known as the Lumley triangle, to characterize the turbulence state. According to Lumley's analysis, all realizable turbulent flow corresponds to a point inside the map and the special turbulence states occur at its vertices. The computed anisotropy invariant map at location E_1 is given in Fig. 22, exhibiting a typical characteristic of zero-pressure-gradient compressible TBL. A two-component turbulence state in the near wall region is clearly identified and the anisotropy exhibits a maximum value in the buffer layer at $y_n^+ \approx 9.6$, consistent with previous findings of Grilli *et al.* [38] and Pirozzoli *et al.* [33]. In the outer region, the evolution path turns and turbulence gradually develops along an axisymmetric expansion state, approaching an isotropic state at the boundary layer edge.

To assess turbulence evolution, we discuss the anisotropy invariant maps at various streamwise locations E_2-E_4 for DC1and DC4, as reported in Fig. 23. Obviously, remarkable differences are observed between the two cases. For DC1, since the selected three positions are all located in the separation bubble (see Fig. 8), the anisotropy invariant maps share a similar behavior. As shown in Fig. 23(a, c, e), turbulence in the proximity of the wall at locations E_2-E_3 gradually approaches to a two-component axisymmetric state, followed by a reversal tendency at location E_4. In the near-wall region, the anisotropy experiences a considerable reduction due to the adverse pressure gradient and moves closer to the axisymmetric compression limit, exhibiting a tendency toward the isotropic, as previously observed by Grilli *et al.* [38] in the separated flow of STBLIs in a compression-expansion ramp. Moreover, an axisymmetric compression state is observed in the region of $0.3 < y_n/\delta_{ref} < 0.6$, corresponding to the presence of the separated shear layer.

For DC4, despite the flow at location E_2 is characterized by the separation, the results in Fig. 23(b) exhibit a substantially different behavior. Close to the wall, the anisotropy first decreases and then increases rapidly, attaining a maximum value at $y_n/\delta_{ref} = 0.06$. Further away from the wall, a gradually reduction of the anisotropy is seen and most turbulence states evolve along the axisymmetric expansion limit toward isotropic conditions, which closely resembles those of the upstream TBL. These discrepancies between the two cases are likely related to the significant reduction of the bubble size with increasing L_c. Recalling Fig. 9, the comparison of bubble size between DC1 and DC4 at location E_2 highlights a drastic reduction of 91%, suggesting that the effect of the separation in DC4 is rather weak, which also explains the

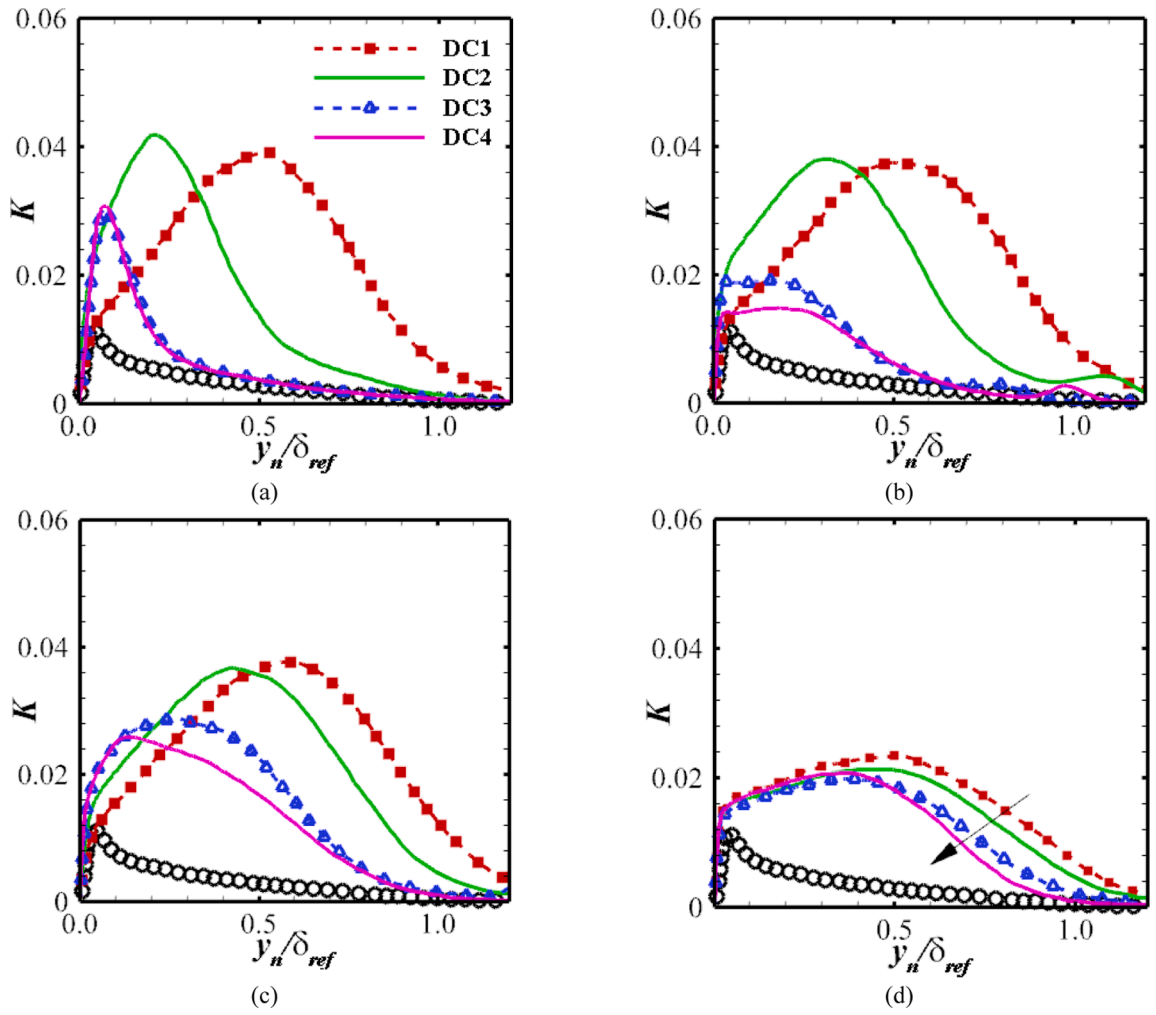

Fig. 21. Distributions of turbulence kinetic energy at various streamwise locations: (a) E2; (b) E3; (c) E4; (d) E5. Open circles refer to the results taken at E_1.

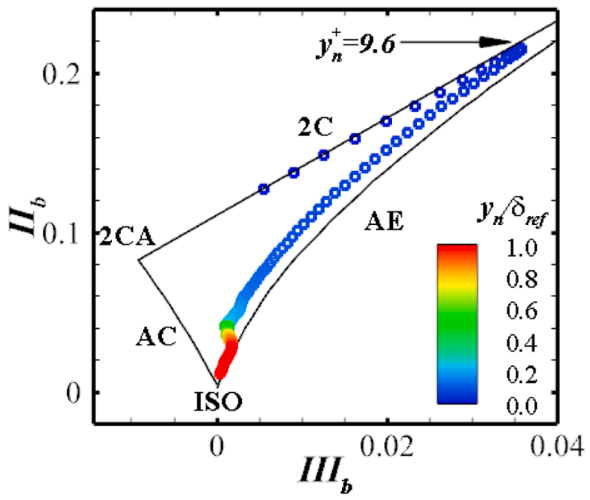

Fig. 22. Anisotropy invariant map at location E_1. ISO: isotropic; AC: axisymmetric compression; 2CA: two-components axisymmetric; AE: axisymmetric expansion; 2C: two-components.

notable changes only observed in the vicinity of the wall. At location E_3, it can be seen from Fig. 23(d) that the reattached flow undergoes a decrease of anisotropy for $y_n/\delta_{ref} < 0.3$, having its maximum value at $y_n/\delta_{ref} = 0.02$. It is worth pointing out that a reversal tendency along the two-component limit is clearly observed in the region very close to the wall, consistent with the recovery process appeared in the inner layer. At location E_4, Fig. 23(f) shows that the anisotropy of the flow in the near-wall region is further decreased and becomes closer to the axisymmetric compression state, whereas turbulence in the outer region experiences a significant increase, mostly following the axisymmetric expansion limit.

In Fig. 24, the anisotropy invariant maps at location E_5 for all cases are quantitatively compared to provide further information. Apparently, the results in the near-wall region collapse very well, which is in accordance with the Reynolds stress components in Fig. 20 and TKE in Fig. 21. Moreover, the anisotropy attains a local peak at $y_n/\delta_{ref} = 0.013$, implying the occurrence of the flow recovery process in the inner layer. Although no collapse is found in the outer region, turbulence for all cases is mostly characterized by the axisymmetric expansion limit. This behavior is also observed by Pirozzoli *et al.* [33] and Grill *et al.* [38] in the downstream region of the interaction with the shock wave. In contrast to significant variations of turbulence evolution across the interaction region, the anisotropy downstream of the interaction seems to be less affected by increasing L_c. The reasons for this phenomenon might be attributed to the faster recovery in the near-wall region of the reattachment boundary layer and the survived large-scale structures in the outer region. Recalling Fig. 20(d, h, l) and Fig. 12, it is reasonably speculated that increasing L_c leads to a stronger weakness of these structures, but do not essentially change its character.

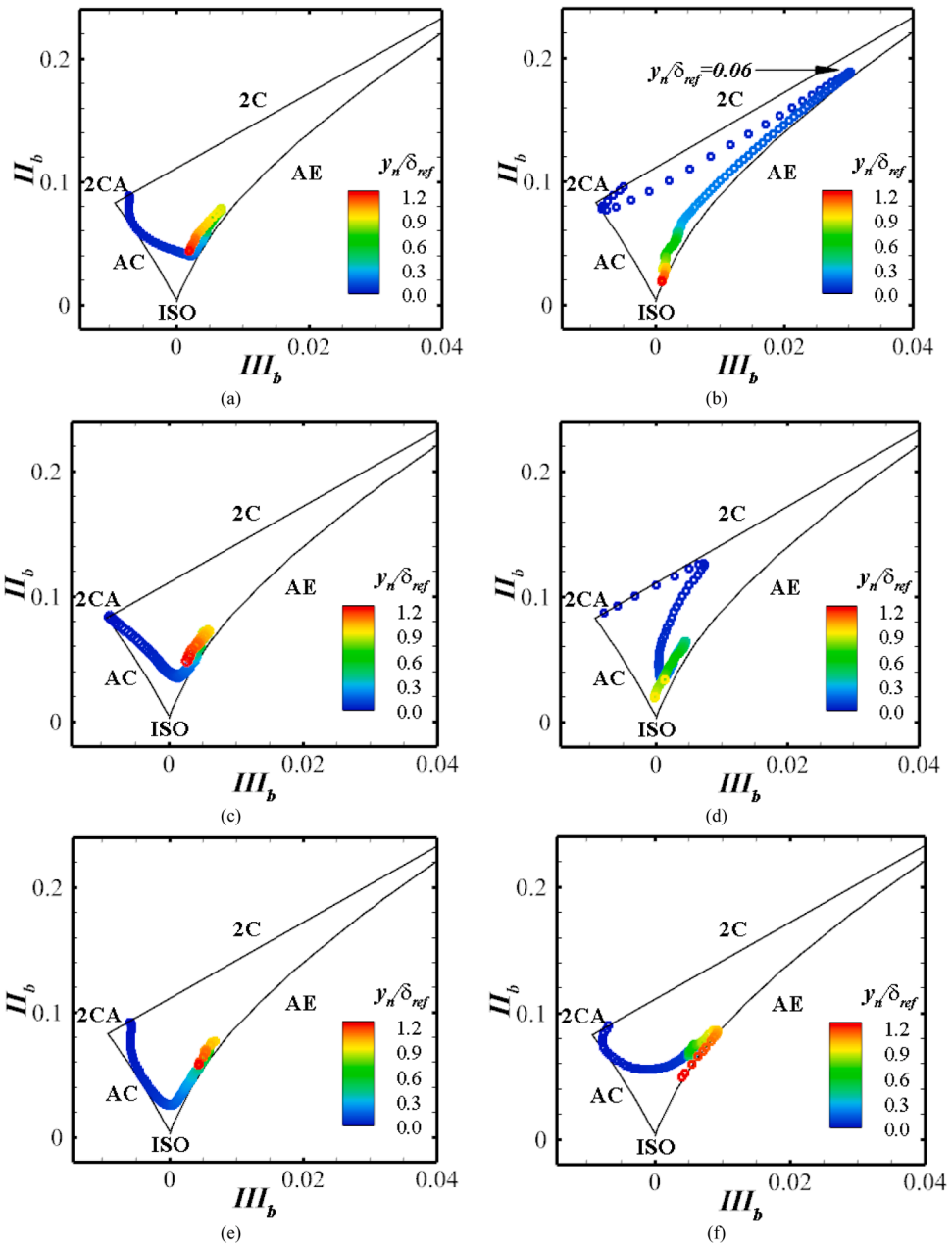

Fig. 23. Anisotropy invariant maps at various streamwise locations: (a, b) E_2; (c, d) E_3; (e, f) E_4. Left: DC1; right: DC4. Refer to Fig.22 for the abbreviation.

4. Conclusions

In the present study, direct numerical simulations of shock wave and turbulent boundary layer interactions in double compression ramps with α_1 =12° and α_2 = 24° at Mach 2.9 are carried out. The characteristic features of the shock interactions, including flow structures, shock unsteadiness, and turbulence evolution, are significantly affected by increasing the distance between the two kinks. Increasing L_c while keeping the ramp angles α_1 and α_2 constant leads to a considerable decrease in the size of the separation bubble, and a complicated shock system. The presence of the second ramp is responsible for the increased streamline curvature and the occurrence of Görtler-like vortices is promoted downstream of the interaction. An increase of L_c results in decreased spanwise width and increased spanwise coherency of these counter-rotating streamwise vortices. Despite the local wall pressure is strongly changed, the total adverse pressures gradient across the interaction is found to be insensitive to L_c. The pre-multiplied spectra of fluctuating wall pressure at mean separation point evidence a suppression of low-frequency unsteadiness, and the shock motion is mainly characterized by high-frequency fluctuations. The streamwise evolution of turbulence throughout the interaction is significantly altered in the near-wall region and in the outer region due to decreased bubble size and different shock pattern. The decreased anisotropy in the near wall region approaches to the axisymmetric compression state, in contrast to the axisymmetric expansion state in the outer layer. Downstream of the interaction, the inner layer experiences a faster recovery and a local peak of turbulence anisotropy is observed. However, turbulence in the outer layer undergoes a monotonic decay and tends to move towards the wall as L_c is increased, while the turbulence anisotropy is less affected and mostly characterized by the axisymmetric expansion limit.

Author Statements

Tong Fulin: Conceptualization, Formal analysis

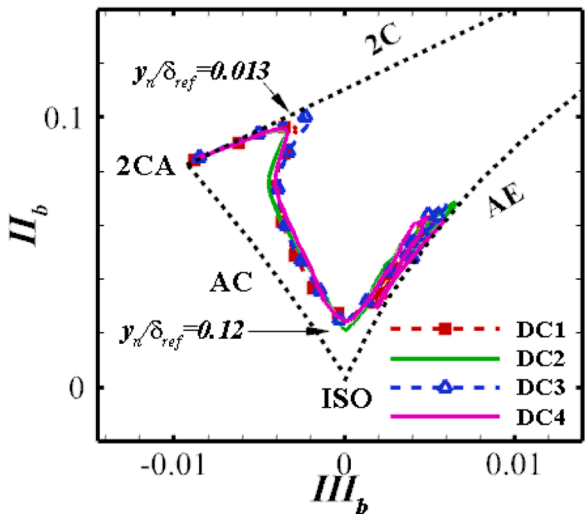

Fig. 24. Anisotropy invariant map at location E_5. Refer to Fig.22 for the abbreviation.

Duan Junyi: Validation, Writing- Original draft preparation
Li Xinliang: Conceptualization, Writing- Reviewing and Editing

Declaration of Competing Interest

We declare that we have no financial and personal relationships with other people or organizations that can inappropriately influence our work; there is no professional or other personal interest of any nature or kind in any product, service and/or company that could be construed as influencing the position presented in, or the review of, the manuscript entitled.

Acknowledgments

This work was supported by NSFC Projects (Nos. 11972356 and 91852203), the National Key Research and Development Program of China (2019YFA0405300). The authors thank National Supercomputer Center in Tianjin (NSCC-TJ), and National Supercomputer Center in Guangzhou (NSCC-GZ) for providing computer time.

References

[1] Dolling DS. Fifty years of shock-wave/boundary-layer interaction research: what next. AIAAJ 2001;39(8):1517–31.
[2] Gaitonde DV. Progress in shock wave/boundary layer interactions. Prog Aerosp Sci 2015;72:80–99.
[3] Settles GS, Fitzpatrick TJ, Bogdonoff SM. Detailed study of attached and separated compression corner flowfields in high Reynolds number supersonic flow. AIAAJ 1979;17(6):579–85.
[4] Ardonceau PL. The structure of turbulence in a supersonic shock-wave/boundary-layer interaction. AIAAJ 1984;22(9):1254–62.
[5] Mustafa MA, Parziale NJ, Smith MS, Marineau EC. Amplification and structure of streamwise-velocity fluctuations in compression-corner shock-wave/turbulent boundary-layer interactions. J Fluid Mech 2019;863:1091–122.
[6] Tong FL, Yu CP, Tang ZG, Li XL. Numerical studies of shock wave interactions with a supersonic turbulent boundary layer in compression corner: Turning angle effects. Comput Fluids 2017;149:56–69.
[7] Muck KC, Andreopoulos J, Dussauge JP. Unsteady nature of shock-wave/turbulent boundary-layer interaction. AIAAJ 1988;26(2):179–87.
[8] Sun ZZ, Gan T, Wu Y. Shock-wave/boundary-layer interactions at compression ramps studied by high-speed schlieren. AIAAJ 2020;58(4):1681–8.
[9] Clemens NT, Narayanaswamy V. Low -frequency unsteadiness of shock wave/turbulent boundary layer interactions. Annu Rev Fluid Mech 2014;46(1):469–99.
[10] Goldfeld MA, Zakharova YV, Fedorova NN. Investigation of separation properties of turbulent boundary layer at its sequential interaction with shock of different strenths. Thermophys Aeromech+ 2008;15(3):453–61.
[11] Gaisbauer U, Knauss H, Fedorova NN, Kharlamova YV. Experimental and numerical investigation of shock /turbulent boundary-layer interaction on a double ramp configuration. editors. In: Rath HJ, Holze C, Heinemann HJ, Henke R, editors. New results in numerical and experimental fluid mechanics V. Contributions to 14th STAB/DGLR symposium; 2004. p. 297–304.
[12] Chapman DR, Kuehn DM, HK Larson. Investigation of separated flows in supersonic and subsonic streams with emphasis on the effect of transition. NACA Report 1957:1356.
[13] Fedorchenko IA, Fedorova NN, Kharlamova YV, Gaisbauer U, Kraemer E. Numerical simulation of supersonic flow around a double ramp configuration and correlation with experiment. Computational fluid dynamics 2006. Proceedings of the fourth international conference on computational fluid dynamics, p. 683–688.
[14] Adams NA. Direct numerical simulation of turbulent boundary layer along a compression ramp at M=3 and Re_θ=1685. J Fluid Mech 2000;420:47–83.
[15] Wu M, Martin MP. Direct numerical simulation of supersonic turbulent boundary layer over a compression ramp. AIAA J 2007;45(4):879–89.
[16] Wu M, Martin MP. Analysis of shock motion in shock wave and turbulent boundary layer interaction using direction numerical simulation data. J Fluid Mech 2008;594:71–83.
[17] Priebe S, Martin MP. Low-frequency unsteadiness in shock wave-turbulent boundary layer interaction. J Fluid Mech 2012;699:1–49.
[18] Priebe S, Tu JH, Rowley CW, Martin MP. Low-frequency dynamics in a shock-induced separated flow. J Fluid Mech 2016;807:441–77.
[19] Zhu XK, Yu CP, Tong FL, Li XL. Numerical study on wall temperature effects on shock wave/turbulent boundary-layer interaction. AIAA J 2017;55(1):131–40.
[20] Tong FL, Tang ZG, Yu CP, Zhu XK, Li XL. Numerical analysis of shock wave and supersonic turbulent boundary interaction between adiabatic and cold walls. J Turbul 2017;18(6):569–88.
[21] Li XL, Fu DX, Ma YW, Liang X. Direct numerical simulation of compressible turbulent flows. Acta Mech. Sin 2010;26:795–806.
[22] Tong FL, Li XL, Duan YH, Yu CP. Direct numerical simulation of supersonic turbulent boundary layer subjected to a curved compression ramp. Phys Fluids 2017;29:125101.
[23] Tong FL, Li XL, Yuan XX, Yu CP. Incident shock wave and supersonic turbulent boundary layer interactions near an expansion corner. Comput Fluids 2020;198:104385.
[24] Martin MP, Taylor EM, Wu M, Weirs VG. A bandwidth-optimized WENO scheme for the effective direction numerical simulation of compressible turbulence. J. Comput. Phys 2006;220:270–89.
[25] Pirozzoli S, Grasso F, Gatski TB. Direct numerical simulation and analysis of a spatially evolving supersonic turbulent boundary layer at M=2.25. Phys Fluids 2004;16:530.
[26] Spalart PR. Direct simulation of a turbulent supersonic boundary layers up to Re_θ=1410. J. Fluid Mech 1988;187:61–98.
[27] Duan L, Beekman I. Direct simulation of hypersonic turbulent supersonic boundary layers. Part 3. Effect of Mach number. J. Fluid Mech 2011;672:245–67.
[28] Del Alamo JC, Jimenez J. Spectra of the very large anisotropic scales in turbulent channels. Phys Fluids 2003;15:L41–4.
[29] Elena M, Lacharme J. Experimental study of a supersonic turbulent boundary layer using a laser Doppler anemometer. J Mec Theor Appl 1988;7:175–90.
[30] Pirozzoli S, Bernardini M, Grasso F. Characterization of coherent vortical structures in a supersonic turbulent boundary layer. J Fluid Mech 2008;613:205–31.
[31] Schlatter P, Orlu R. Assessment of direct numerical simulation data of turbulent boundary layers. J Fluid Mech 2010;659:116–26.
[32] Sun MB, Sandham N D, Hu ZW. Turbulence structures and statistics of a supersonic turbulent boundary layer subjected to concave surface curvature. J Fluid Mech 2019;865:60–99.
[33] Pirozzoli S, Bernardini M, Grasso F. Direct numerical simulation of transonic shock/boundary layer interaction under conditions of incipient separation. J Fluid Mech 2010;657:361–93.
[34] Garnier E, Sagaut P, Deville M. Large-eddy simulation of shock/boundary-layer interaction. AIAA J 2002;40(10):1935–44.
[35] Jeong J, Hussain F. On the identification of a vortex. J Fluid Mech 1995;285:69–94.
[36] Dawson DM, Lele SK. Large eddy simulation of a three-dimensional compression ramp shock-turbulent boundary layer interaction. Reston: AIAA; 2015. Report No.: AIAA-2015-1518.
[37] Loginov MS, Adams NA, Zheltovodov AA. Large-eddy simulation of shock-wave/turbulent-boundary-layer interaction. J Fluid Mech 2006;565:135–69.
[38] Grilli M, Hickel S, Adams NA. Large-eddy simulation of a supersonic turbulent boundary layer over a compression-expansion ramp. Intl J Heat Fluid Flow 2013;42:79–93.
[39] Smits AJ, Dussauge JP. Turbulent shear layers in supersonic flow. 2nd end. Springer; 2006.
[40] Theisel H. Vector field curvature and applications. Unviersity at Rostock; 1995. Ph. D. Thesis.
[41] Pasquariello V, Hickel S, Adams NA. Unsteady effects of strong shock-wave/boundary-layer interaction at high Reynolds number. J Fluid Mech 2017;823:617–57.
[42] Bernardini M, Asproulias I, Larsson J, Pirozzoli S, Grasso F. Heat transfer and wall temperature effects in shock-wave/turbulent boundary-layer interactions. Phys Rev Fluids 2016;1(8):084403.
[43] Fang J, Yao YF, Zheltovodov AA, ZR Li, Lu LP. Direct numerical simulation of supersonic turbulent flows around a tandem expansion-compression corner. Phys Fluids 2015;27:125104.
[44] Lumley JL. Computational modeling of turbulent flows. Adv Appl Mech 1978;18:123–76.